Journal of Materials Science & Technology 50 (2020) 192–203

Contents lists available at ScienceDirect

Journal of Materials Science & Technology

journal homepage: www.jmst.org

Research Article

Achieving work hardening by forming boundaries on the nanoscale in a Ti-based metallic glass matrix composite

Jing Fan[a,b], Wei Rao[c], Junwei Qiao[a,b,*], P.K. Liaw[d], Daniel Şopu[e,f], Daniel Kiener[g], Jürgen Eckert[f,g], Guozheng Kang[c], Yucheng Wu[a,**]

[a] College of Materials Science and Engineering, Taiyuan University of Technology, Taiyuan, 030024, China
[b] Key Laboratory of Interface Science and Engineering in Advanced Materials, Ministry of Education, Taiyuan University of Technology, Taiyuan, 030024, China
[c] Key Laboratory of Advanced Technologies of Materials, School of Mechanics and Engineering, Southwest Jiaotong University, Ministry of Education of China, Chengdu, 610031, China
[d] Department of Materials Science and Engineering, The University of Tennessee, Knoxville, TN, 37996-2200, USA
[e] Technische Universität Darmstadt, Institut für Materialwissenschaft, Fachgebiet Materialmodellierung, Otto-Berndt-Strasse 3, D-64287, Darmstadt, Germany
[f] Erich Schmid Institute of Materials Science, Austrian Academy of Sciences, Jahnstraße 12, A-8700, Leoben, Austria
[g] Department of Materials Science, Montanuniversität Leoben, Jahnstraße 12, A-8700, Leoben, Austria

ARTICLE INFO

Article history:
Received 21 December 2019
Accepted 20 February 2020
Available online 19 March 2020

Keywords:
Metallic glass matrix composites
Plastic deformation
Work hardening
Dense dislocation walls
Nanoscale boundaries

ABSTRACT

Achieving work hardening in metallic glass matrix composites (MGMCs) is the key to the extensive use of these attractive materials in structural and functional applications. In this study, we investigated the formation of nanoscale boundaries resulted from the interaction between matrix and dendrites, which favors the work-hardening deformation in an *in-situ* $Ti_{41}Zr_{32}Ni_6Ta_7Be_{14}$ MGMC with β-Ti dendrites in a glassy matrix at room temperature. The microstructures of samples after tension were observed by high-resolution transmission electron microscopy (HRTEM) and X-ray diffraction (XRD). The work-hardening mechanism of the present composites involves: (1) appearance of dense dislocation walls (DDWs), (2) proliferation of shear bands, (3) formation of boundaries on the nanoscale, and (4) interactions between hard and soft phases. A theoretical model combined with experimental data reveals the deformation mechanisms in the present work, proving that the *in-situ* dendrites with outstanding hardening ability in the glass matrix can provide the homogeneous deformation under tensile loading at room temperature.

1. Introduction

Bulk metallic glasses (BMGs) possess the potential to be used as structural materials for a variety of applications due to their outstanding mechanical, chemical, and physical properties [1,2]. Unfortunately, they usually exhibit a brittle-fracture behavior under freestanding loading conditions at room temperature, such as upon the uniaxial tension [3]. Significant efforts have been made to overcome this shortcoming in recent years with the development of metallic glass matrix composites (MGMCs), consisting of ductile crystals precipitated *in-situ* in a glass-forming matrix [4]. The existence of crystals within the amorphous matrix hinders the rapid propagation of shear bands, and favors shear band blocking and multiplication. The formation of a highly organized pattern of multiple shear bands which, in turn, interact in a very complex way with each other and the crystals retards the early failure of MGMCs and ensures improved ductility.

Previous studies have introduced various MGMCs with excellent room-temperature tensile ductility [5–7]. Unfortunately, most of these composites exhibit macroscopic-strain softening with early onset of necking ascribed to a lack of work-hardening capacity, which restricts the structural applications for such kinds of *in-situ* MGMCs [8,13]. Because of this challenge, transformation-induced plasticity (TRIP) [7,9] and twining-induced plasticity (TWIP) [14] mechanisms have been employed in MGMCs through controlling their compositions, and concomitant work hardening has been realized in MGMCs. For example, B2-type MGMCs containing spherical polymorphous B2 CuZr/Ti precipitates [7,9] and β-type

* Corresponding author at: College of Materials Science and Engineering, Taiyuan University of Technology, Taiyuan, 030024, China.
** Corresponding author.
E-mail addresses: qiaojunwei@gmail.com (J. Qiao), wyc@tyut.edu.cn (Y. Wu).

https://doi.org/10.1016/j.jmst.2020.02.036
1005-0302/

primary β-Zr/Ti solid solution dendrites embedded in a glassy matrix [10–12] are two common *in-situ* MGMCs. The metastable B2 CuZr phase undergoes martensitic phase transformation during plastic straining, which produces excellent room-temperature plasticity and work-hardening capacity through TRIP effect [7].

In addition to the work-hardening mechanisms of MGMCs under tension referred before, the novel *in-situ* Ti-based MGMCs, presented in this study, show distinct tensile ductility with significant work-hardening capability, which is ascribed to the formation of nanoscale boundaries at interface between the dendrites and the matrix. The generation of boundaries on the nanoscale is based on the formation of DDWs within the dendrites, and develops with the interplay between shear bands in the matrix and DDWs. With the help of finite element modeling (FEM), digital-image correlation (DIC), nanoindentation tests, as well as high-resolution transmission electron microscopy (HRTEM), it is well proved that the ductile dendrites with remarkable work-hardening capacity act as a prerequisite for achieving uniform elongation of the MGMCs. The deformation mechanisms are explored by accounting for the competition between the matrix and the dendrites upon tensile loading. The generation of dense dislocation walls (DDWs) and the development of boundaries on the nanoscale in dendrites during tension induce remarkable work- hardening behavior. On the other side, the nucleation and propagation of shear bands within matrix lead to softening. Moreover, a model has been developed to study the deformation behavior of the composites. The work-hardening coefficients "n" and "n'" obtained through the model indicate that the hardening originated from boundaries on the nanoscale in the dendrites and softening induced by shear banding within the glass matrix, respectively. The experimental results together with the developed constitutive relations clearly unveil the work-hardening mechanisms of such kinds of composites. Hence, the current findings extend the fundamental understanding of the deformation mechanisms of MGMCs upon tension, and pave a way to design MGMCs with significant uniform elongation at room temperature.

2. Experimental

The *in-situ* $Ti_{41}Zr_{32}Ni_6Ta_7Be_{14}$ [atomic percent (at.%)] MGMCs specimens were prepared by arc melting the mixture of pure elements [purity >99.9 wt percent (wt.%)], Ti, Zr, Ni, Ta, and Be, under a Ti-gettered argon atmosphere. The ingots were re-melted at least four times in a high-purity argon atmosphere to ensure chemical homogeneity. Copper-mold-casting was used to fabricate plate-shape samples. The size of the samples was 2 mm in thickness and 10 mm in width. The structures of phases in the as-cast ingots were characterized by X-ray diffraction (XRD; Ultimalv) with Cu-K_α radiation. Microstructures and chemical compositions were analyzed by scanning electronic microscopy (SEM; TESCAN, LYRA 3 XMH) combined with energy-dispersive spectrometry (EDS). The tensile samples, which have been cut into a shape of dog -bone-like (10 mm (length) ×2 mm (width) ×2 mm (thickness)). The tensile experiments at room temperature were conducted with an Instron 5969 testing machine at a strain rate of 5×10^{-4} s^{-1}. To confirm the reproducibility of the tests, at least three specimens were tested. The evolution of local strains during the experiments was detected by digital image correlation (DIC) using the MatchID system. For these tests, white paint was sprayed on one side of the samples and then coated with black spots in order to increase the contrast of the images taken during the DIC experiments. XRD, SEM, transmission electron microscopy (TEM), and HRTEM in a JEM-2010 microscope were performed to check the failed samples. Mechanical grinding was the first step when preparing the TEM specimens, followed by ion milling (ion energy: 4.5–5 keV) with Gatan 691 Polisher. The hardness and Young's modulus required in the present work were calculated from nanoindentation tests (MTS Systems, USA). Computational micromechanics investigation on the formation and evolution of deformation bands have been developed in the current work. The deformation behavior of monolithic BMGs is generally described by the free-volume model and the mechanism-based strain-gradient plasticity model [15–17], which are described in a model with a finite element code (ABAQUS) as user material subroutines. The shear bands in the glass matrix and the slip bands in the dendrites, which are induced by the concentration of free volumes and pile-ups of dislocation, respectively, are internal state variable SDV1 in the code. In the current work, a two-dimensional (2-D) plane-strain finite element model (FEM) was chosen. As in a similar model in previous work by Rao et al. [15,17], the loading boundary in this model was perpendicular to the loading direction. The normal constraints appear opposite to the loading boundary, and the full constraints appear at a vertex of the opposite boundary.

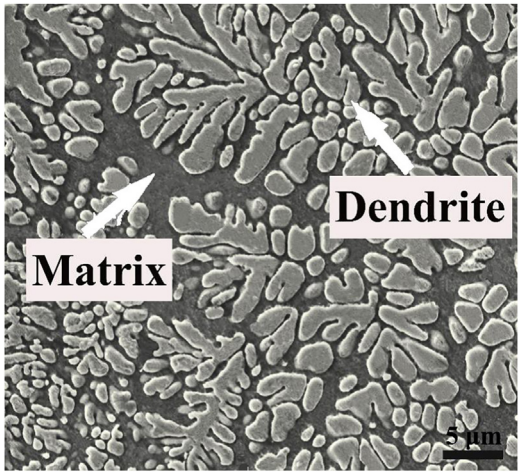

Fig. 1. SEM image of the as-cast composite.

Table 1
Contents of different elements in the present Ti-based MGMCs (in at.%).

Zone	Ti	Zr	Ni	Ta	Be
Composite	41	32	6	7	14
Matrix	34.8 ± 0.2	47.2 ± 2.1	12.4 ± 1.8	5.6 ± 0.2	–
Dendrites	47.2 ± 0.5	34.8 ± 2.0	4.0 ± 1.7	14.0 ± 0.4	–

3. Results

Fig. 1 shows the result from SEM observations for the as-cast $Ti_{41}Zr_{32}Ni_6Ta_7Be_{14}$ composites. *In-situ* dendrites are continuously distributed within the glassy matrix, as denoted by the arrows. The volume fraction of the dendrites and the average width of the dendrite arm were evaluated by the Image pro software from the SEM images, and the values are 49 ± 3 vol.% and 1–2 μm, respectively. In order to clarify the chemical compositions of both phases, the content of the elements Ti, Zr, Ni, and Ta was acquired by EDS analysis. Be is hard to detect precisely, since it is very light and completely dissolved in the amorphous matrix [18]. Table 1 presents the chemical compositions of both phases. The values given for the composition in the first line correspond to the nominal composition. The glass matrix is enriched in Zr and Ni and the dendrites in Ti and Ta, similar to others developed *in-situ* Ti-based MGMCs [10].

The TEM images of an as-cast sample are shown in Fig. 2 to reveal the details of the microstructure. As can be found from Fig. 2(a), bright elliptical particles and gray regions correspond to the dendrites and matrix, respectively. The selected-area electron diffraction (SAED) patterns displayed in Fig. 2(b) and (c) correspond

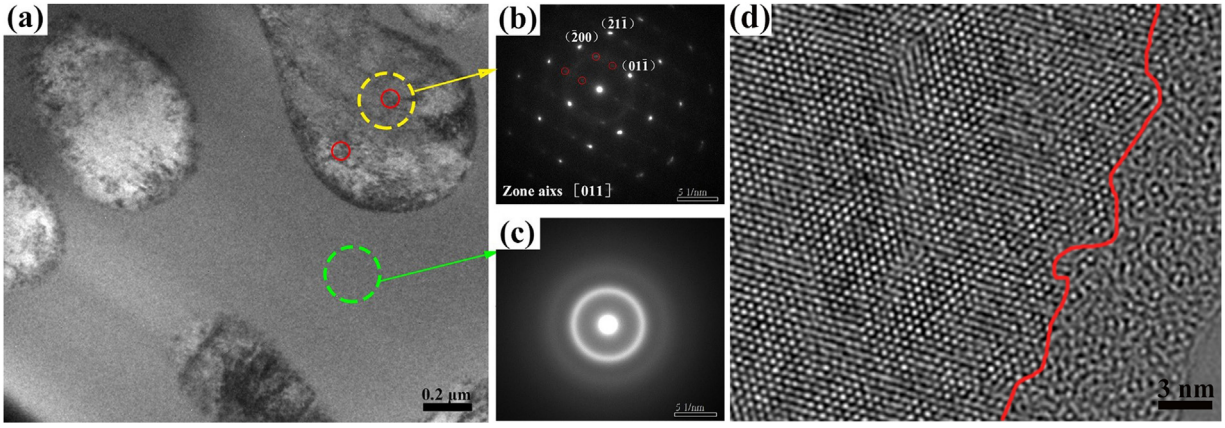

Fig. 2. TEM images of the as-cast sample: (a) bright-field TEM image, selected-area electron diffraction (SAED) patterns of the dendrites and the matrix are presented in (b) and (c), respectively, (d) the HRTEM image of the interface.

to the yellow and green regions in Fig. 2(a), respectively, and convincingly demonstrate the formation of the body-centered-cubic (bcc) β-Ti dendrites and the amorphous matrix. Besides the diffraction spots from the β-Ti solid solution, additional weak diffraction spots indicated by red circles, corresponding to the red circles in Fig. 2(a), at 1/3 $\{112\}_\beta$ and 2/3 $\{112\}_\beta$ are visible [19]. Among several binary and multi-component Ti and Zr alloys, the ω phase may appears when the stability of the β phase is enhanced by adding β stability elements, such as Mo, Co, and Ta [20]. Consequently, these spots can be identified as ω-Ti, which is formed by a displacive shuffle dominated mechanism during rapid cooling [20]. However, the structure of ω-Ti cannot be observed in XRD and SEM, which means the amount of ω-Ti is very small or can be almost neglected. Fig. 2(d) shows the HRTEM image of the as-cast sample, which displays the interface between the dendrites and the matrix. It can be seen that the atomic bonding, shown by the red line, between the two phases are very good, no obvious defects and stress concentration happened in this place. The deformation mechanisms are closely related to the intrinsic composition of the composites. In particular, special attention has been directed towards the Ti-based alloys developed by adding β-phase or α-phase stabilizing elements [20]. In view of MGMCs, thermos-mechanical processing of Ti-based alloys (the dendrites) involves deformation in the different phases depending on the compositions and the change of the β-phase stabilizer (Ta) in the dendrites affects the phase stability, which influences the structure and deformation mechanisms of MGMCs upon loading [20,21].

The XRD patterns of as-cast and deformed samples are shown in Fig. 3. Sharp peaks, denoting crystalline phases, can be found to be superimposed on a broad diffuse diffraction background corresponding to the amorphous phases, indicating the concomitant existence of bcc β-Ti and amorphous phases, respectively. The XRD patterns after tensile deformation exhibit the same set of diffraction peaks and no additional peaks, confirming that there is no phase transformation upon plastic deformation.

Fig. 4(a) displays a characteristic tensile true stress-true strain curve of the composite at ambient temperature. Apparently, the MGMC exhibits a distinct work-hardening behavior. It yields at 1200 ± 45 MPa, followed by a region with increasing flow stress, and finally reaches an ultimate tensile strength (UTS) of 1640 ± 37 MPa and a total uniform strain of 5%. The plastic deformation is susceptible to localized deformation (necking), and the Considére criterion can be used to detect necking [22].

$$\frac{d\sigma}{d\varepsilon} \leq \sigma \qquad (1)$$

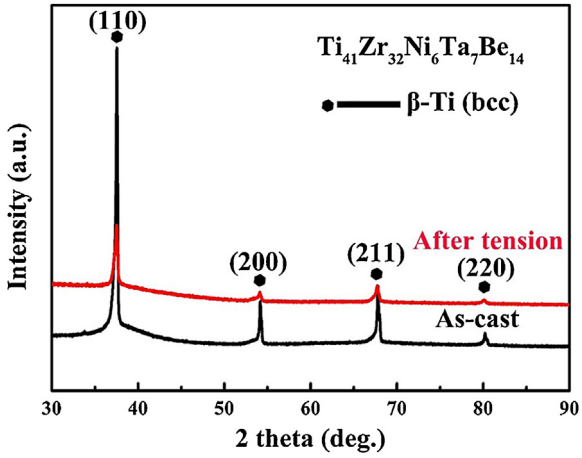

Fig. 3. XRD patterns of the composite before and after tensile deformation.

where, σ, is the true stress, and, ε, is the true strain. The work-hardening rate ($d\sigma/d\varepsilon$) calculated from the true stress-true strain curve is shown in the inset of Fig. 4(a). Comparing these two curves in Fig. 4(a) reveals that necking does not happen until final fracture, and the value of the work-hardening rate exceeds the tensile stress during the whole plastic deformation stage. In other words, the significant work hardening without macroscopic necking dominates when the composite is subjected to tensile straining. The different slopes shown in the *C-J* plot ($d\sigma/d\varepsilon$ vs. ε) provide insight into possible changes in the deformation mechanisms. Multi-stage work-hardening behavior, which is common in crystalline alloys with remarkable work-hardening, is evident in the present composite [Fig. 4(a)] [23,24]. The fracture morphology of the samples after tension is displayed in Fig. 4(b). Profuse shear bands indicate the large plastic deformation for the present MGMCs. The inset in Fig. 4(b) presents an image of a fractured sample. Apparently, the tensile failure of the current composite occurs in a shear fracture mode. Three fracture angles (57.7°, 77.6°, and 90°) can be detected on the fracture surface. Zhang et al. have reported that the tensile fracture angle is 54° in monolithic Zr-based BMGs [25]. The tensile fracture angles are larger in the present MGMC, indicating that both normal and shear stresses act on the fracture plane.

The detailed deformation structures in the fractured samples after tension are presented in Fig. 5. Fig. 5(a) and (b) shows the TEM images of a fractured specimen. Compared with as-cast sample shown in Fig. 2(a), DDWs are frequently found within the dendrites along the interface. Fig. 5(c) presents a HRTEM image taken

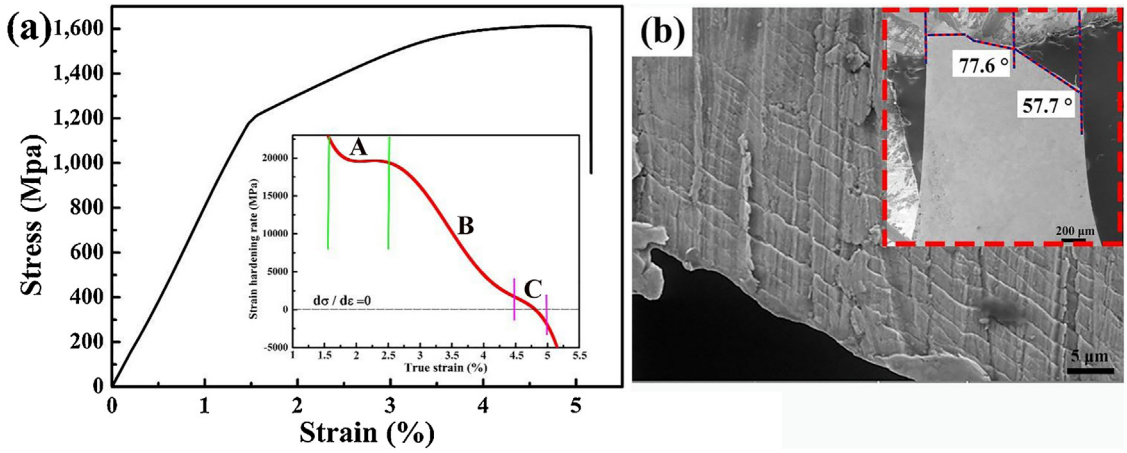

Fig. 4. True stress-true strain curve of the composite (a), the work-hardening rate curve is shown in the inset. (b) SEM images of a sample after fracture.

from the region near the DDWs, where located at the boundary between two phases, represented by red lines in the figure. The red line close to the part of the matrix is the boundary, and the region between two lines belong to the dendrites. It indicates that an irregular nanoscale boundary takes place of the original regular interface (Fig. 2(d)) between two phases during tension. The fast Fourier transform (FFT) patterns inserted at the left-hand bottom side of Fig. 5(c) correspond to the areas of the glass matrix and dendrites, denoted by the squares A and B, respectively. Fig. 5(d) displays a HRTEM image of the glass matrix taken from an area, where a shear band (the light region bordered by red lines) was coincidently caught. The shear band is blocked by a crystal (cf. the ordered lattice within the yellow ellipse).

In crystalline alloys, slips and dislocations are the major carriers of plasticity. In contrast, the plastic deformation in a glassy phase is accommodated by shear bands. Shao et al. have reported that two-zone shear bands (one is a solid-like zone, and the other a liquid-like zone) control the plasticity of metallic glasses [26]. This trend can be inferred from the structure in Fig. 5(d). The generation of a liquid-like zone (the area between the red lines), surrounded by a solid-like zone, is prevented by the crystalline dendrites (the area within the yellow ellipse), which retards the plastic instability. The crystals in MGMCs can hinder or distribute the expansion of shear bands within the matrix. Fig. 5(e) and 5(f) displays magnified HRTEM images of the dendrites. The boundary on nanoscale formed close to the interface is indicated in Fig. 5(e), corresponding to the area between red lines in Fig. 5(c). Dislocations, denoted by "T", severe lattice distortion, represented by yellow circles, and diverse lattice orientations are simultaneously present. The SAED pattern in Fig. 5(e) shows clear diffraction lattice of nanocrystals, which states the structure of the boundary on nanoscale have changed from ordered crystalline lattice to sub-grains and nanocrystal structure. Comparing the HRTEM images of as-cast and fractured samples, as shown in Fig. 2(d) and 5(c), respectively, significant changes on the interface between the dendrites and the matrix have taken place. It indicates that the nanoboundary, consisting of sub-grains and nanocrystal, is formed during tension. The microstructure observed by TEM shown in Fig. 5(e) demonstrates the existence of sub-grains and nanocrystals near boundaries in fractured samples. It is noted that the nanoscale boundary, corresponding the area between red lines in Fig. 5(c), is generated upon straining. Fig. 5(f) depicts the area far away from the boundary. Lattice distortions and dislocations can be observed, corresponding to the inverse FFT image, shown at the left bottom of the figure. The inset in the upper right corner displays the corresponding SAED pattern, which demonstrates that the interior of the dendrites retains the bcc structure for β-Ti solutions, and no phase transformation happens. Consequently, boundaries on the nanoscale are generated within the dendrites close to the interface. The boundaries possess disparate crystalline structure, i.e., neither structure of the glass matrix nor bcc β-Ti of dendrites.

Fig. 6 illustrates the strain increment distribution curve upon tensile loading, as obtained by DIC. Fig. 6(a) shows the strain-distribution maps. And the location of fracture, marked by blue rectangle in Fig. 6(a). The inset shown in Fig. 6(b), was selected for analysis of the temporal strain. The instantaneous strain distribution along loading direction, extracted from the strain-distribution map near the location of fracture, is presented in Fig. 6(b). Obvious necking cannot be found along the gauge length, and the strain increases uniformly during tension except for two inflection points on the instantaneous strain curve at local strains of 0.7% and 2.7%. The above results signify that shear bands generated locally within the glass matrix are arrested by the ductile dendrites, resulting in macroscopically homogenous elongation for the current MGMC.

In order to better understand the deformation behavior, finite element modeling (FEM) was performed. The materials parameters of the glassy and dendrite phases used in the simulation are listed in Table 2. E_m and E_d are elastic modulus of the matrix and dendrites, respectively, ν_m and ν_d are Poisson ratio of the matrix and dendrites, respectively, α, ξ_0, χ, v^*, T, t_0^{-1}, and τ_0 are the geometrical factor, initial free volume concentration within the matrix, geometrical parameter of the matrix, critical volume for the matrix, absolute temperature, characteristic time, and the reference stress of the matrix, respectively. M, b, α, d_p, ψ, $\dot{\varepsilon}_0$, k_{20}, n, N_B, ξ, m_0, and σ_y are Taylor factor, Burgers vector, empirical constant, effective particle size, proportional factor, reference strain rate, dynamic recovery constant, power exponent relating to the dislocation annihilation, maximum number of dislocation loops, viscosity coefficient, and yield strength of the dendrite, respectively.

The inhomogeneous distribution of the stress field is ascribed to the different interactions between two phases when choosing different dendrites. The propagation of shear bands and cracks strongly depends on the mechanical property of the dendrites. In the present FEM model, as shown in the Table 2, the same parameters for the glass matrix were developed and three varied dendrites were chosen as the reinforce phase in the FEM, named by dendrites 1, 2, and 3, respectively. Among three dendrites, materials parameters remain constant except for the M and σ_y. Larger Taylor factor, M_2, was set for the dendrites 2 comparing with the dendrites 1 and 3 ($M_{1,3}$), which ensures work hardening achieved in dendrites 2 upon tension. Higher yield strength, σ_{y3}, was developed for the dendrites 3 comparing with the dendrites 1 and 2 ($\sigma_{y1,2}$),

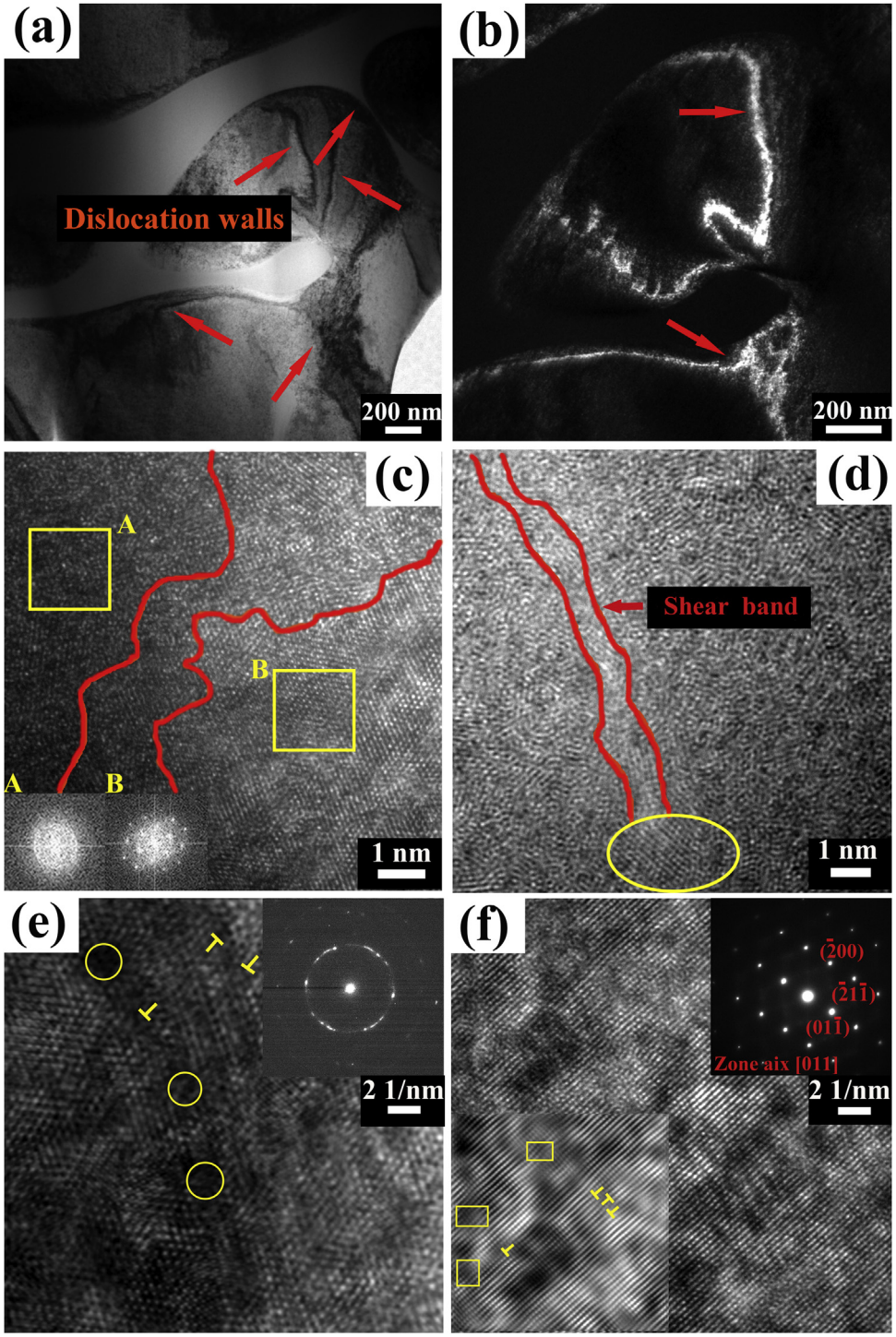

Fig. 5. TEM images of a sample after fracture: (a) bright-field image, (b) dark-field image, (c) HRTEM image of the interface, (d) a shear band in the matrix, (e) and (f) HRTEM images of the dendrites.

Table 2
Material parameters used for the FEM model of the current MGMCs.

Matrix	E_m (GPa)	ν_m	α	ξ_0	χ	v^* (Å)	T (k)	t_0^{-1} (s^{-1})	τ_0 (MPa)
	109.3	0.33	0.8	0.0465	1.25	20	300	324	414

Dendrites	E_d (GPa)	ν_d	$M_{1,3}$	M_2	b (nm)	α	d_p (μm)	ψ	$\dot{\varepsilon}_0$ (s^{-1})	k_{20}	n	N_B	ξ (nm)	m_0	$\sigma_{y1,2}$ (MPa)	σ_{y3} (MPa)
	67	0.36	1.0	2.4	0.256	0.33	2.5	0.2	1	18.5	12.5	45	35	10	900	1200

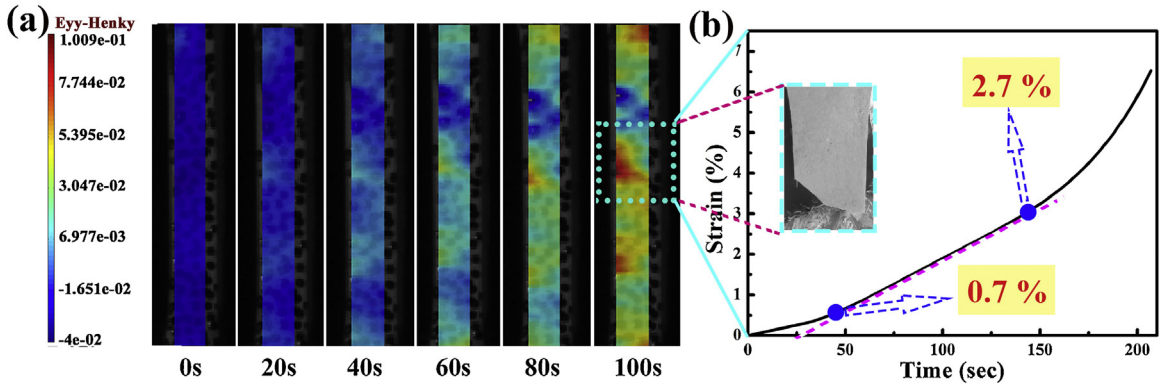

Fig. 6. DIC images of the deformed composite: (a) the strain distribution with time, (b) the corresponding temporal strain curve.

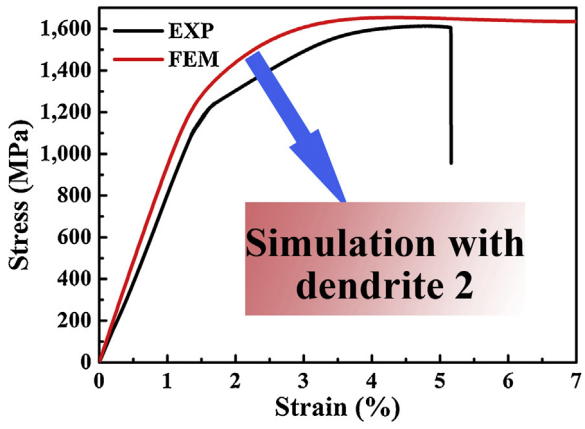

Fig. 7. True stress-true strain curves obtained by the experiment and FEM, respectively.

which intends to observe the deformation behavior of the kind of stronger dendrites. The results indicate that work hardening is not easily achieved even when the reinforce dendrites possess very high strength. And the work hardening results only when the dendrites have remarkable work-hardening capacity. Consequently, the simulation results obtained using dendrites 2 present a similar deformation behavior as the current MGMCs.

The uniaxial tensile stress-strain curves of the *in-situ* MGMC are predicted and compared with the experiments in Fig. 7. The comparison shows a good agreement, indicating that the adopted finite element model is suitable to numerically depict the tensile deformation behavior of the current MGMC reasonably well. Fig. 8(a), (b), and (c) illustrates the evolution of free volume in the glassy matrix, the dislocation density in the dendrites, and the local stress distribution at a strain of 3%. The corresponding values for the late deformation stage, 7%, are shown in Fig. 8(d), (e), and (f), respectively. It is suggested that homogeneous deformation can be found in the present MGMC at the first time when yielding occurs, as displayed by Fig. 8(a), (b), and (c). In contrast, the free volume and the dislocation density rapidly increase at 7% strain, which reveals work softening and hardening in the matrix and dendrites, respectively. What can be observed from Fig. 8(d) and (e) is that the region containing a high concentration of free volume in the matrix [Fig. 8(d)] is adjacent to a region, where the dislocation density is relatively high within the dendrites [Fig. 8(e)]. This trend confirms that the stress concentration at the interface has an effect on the generation of slip bands in the dendrites and on the initiation of shear bands in the amorphous matrix [5]. Fig. 8(f) depicts a map of the strain distribution with respect to the loading direction. Shear localization is not significant. The plastic deformation of the current MGMC under tension is relatively homogenous, as demonstrated in Fig. 8(f). These findings are close to the experimental results.

In addition, another two dendrites were selected to make a comparison with dendrites 2 through the FEM analysis, as shown in Fig. 9. Fig. 9 (a) and (b) demonstrates the results, (a) displaying the stress-strain curves for varied dendrites, and (b) presenting the stress-strain curves of MGMCs with the corresponding dendrites in (a). It is suggested that dendrites 2 exhibit excellent work hardening during deformation, and no hardening behavior can be found in the other two types of dendrites. Consequently, only MGMC 2, with *in-situ* formed dendrites 2 in the amorphous matrix, demonstrates work hardening. For the other two soften dendrites, dendrites 1 with lower yield strength and dendrites 3 with higher one, cannot assist appearance of work hardening in MGMCs, which means that the work-hardening behavior of the dendrites during tension is the necessary factor for achieving work hardening in the corresponding MGMCs. Fig. 10 illustrates the evolution of the free volume within the glassy matrix, the dislocation density in the dendrites, and the local stress distribution at 5% strain for three the MGMCs. Fig. 10(a), (b), and (c) are results of MGMC 1, (d), (e), (f) represent MGMC 2, and (g), (h), and (i) corresponds to MGMC 3. The evolution of free volumes is similar among the three MGMCs [(a), (d), and (g)], which means that the matrix undergoes softening. Obviously, a higher dislocation density forms in MGMC 2 [(b), (e), and (h)]. It is noted that the local stress distribution is more homogenous in MGMCs 2 and 3 when compared to MGMC 1.

4. Discussion

It is well known that the introduction of dendrites into the matrix effectively improve the ductility of BMGs, and the volume friction and size of the dendrites influence the deformation behavior of MGMCs [16]. For the same system MGMCs, the reinforced dendrites act as an important role in deformation mechanism of MGMCs. In other words, the work hardening of MGMCs can be achieved when the reinforced dendrites possess excellent work-hardening ability. In the present MGMC, the dendrites show significant work hardening upon tension, which is induced by the formation of DDWs. The element of Ta works as stabilizer of a β phase in titanium alloys, and TRIP and TWIP effects on the work hardening upon tension among Ti-based MGMCs have been studied [10,14]. Based on the previous studies, fine adjustment of the proportion of Ta and other elements has been conducted. The sub-grain and nanocrystal generated at the interface between two phases is an intermediate state. The composition of the dendrites within MGMCs may determine the deformation mechanism, i.e., the formation of boundary on nano scale stems from the intrinsic property of the present MGMC.

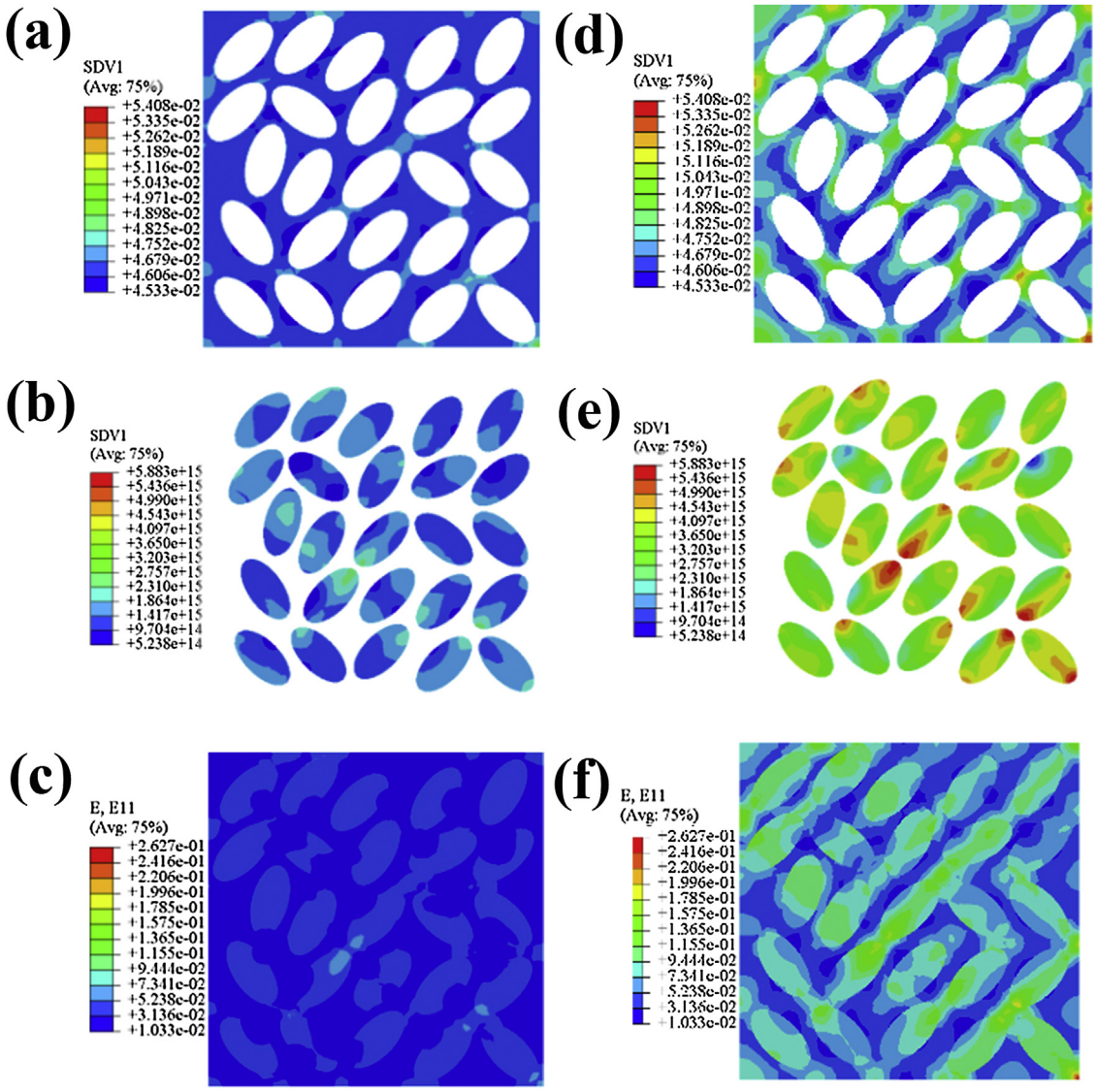

Fig. 8. FEM results obtained at the strain of 3% and 7%: (a) and (d) the evolution of free volumes within the glassy matrix, (b) and (e) the dislocation density in the dendrites, (c) and (f) the local stress distribution.

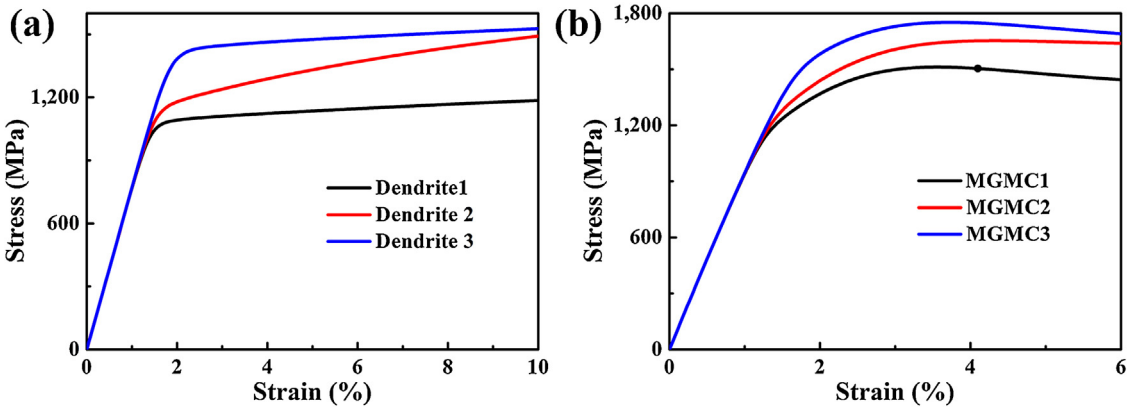

Fig. 9. FEM analysis for another two dendrites: (a) stress-strain curves of different dendrites, (b) stress-strain curves of MGMCs with the corresponding dendrites in (a).

The results described above indicate that boundaries on the nanoscale observed during tension plays an important role in achieving work hardening. Different from TRIP and TWIP deformation mechanisms, the work hardening observed in the present MGMCs is induced by the formation of special nanocrystalline structure. Zhai et al. [27] designed Ti-based MGMCs through adding Sn to tailor the intrinsic properties. Significantly ductile deformation and excellent work hardening can be achieved with Sn

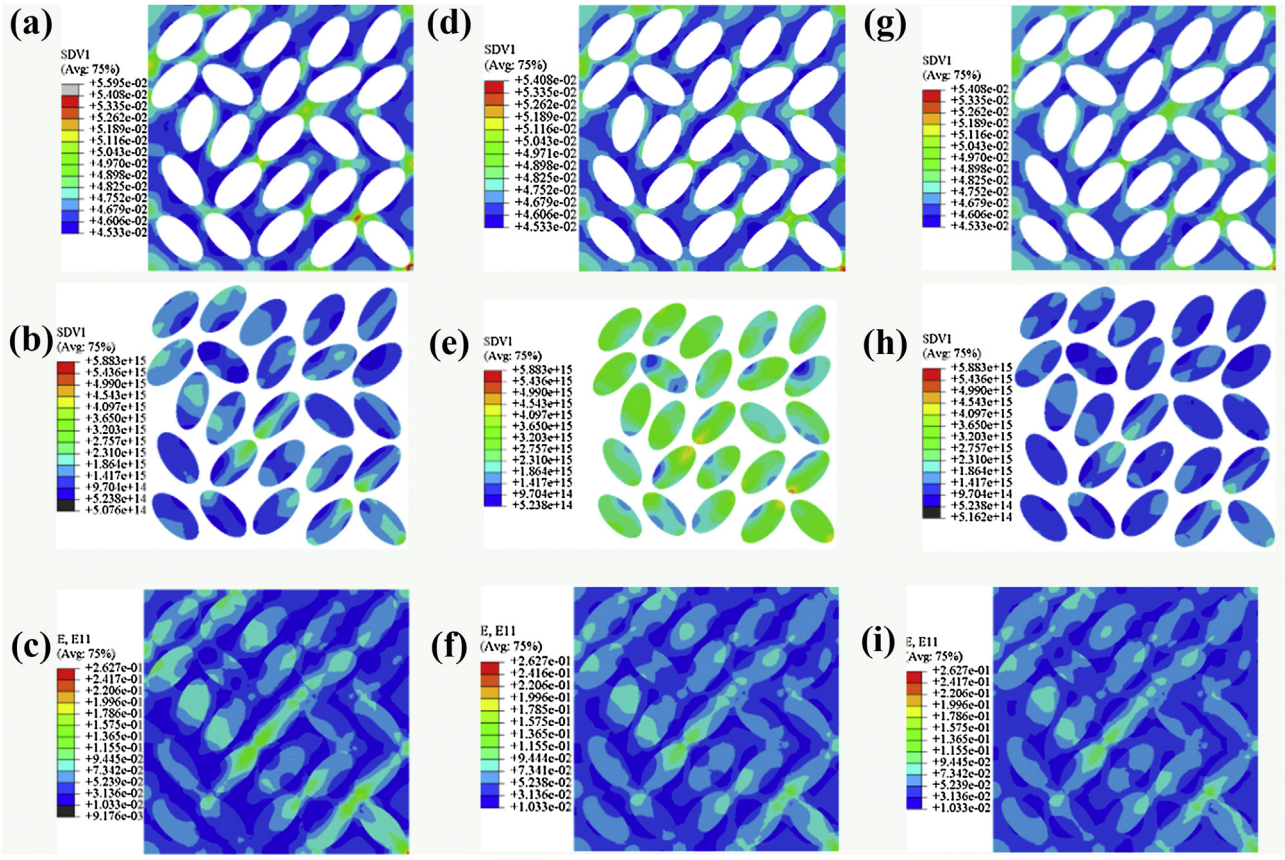

Fig. 10. Evolution of free volumes in the glassy matrix, dislocation density in the dendrites, and local stress distribution at the strain of 5% for three MGMCs: (a), (b), and (c) MGMC 1, (d), (e) and (f) MGMC 2, (g), (h), and (i) MGMC 3.

addition, totally due to dislocation multiplication, similar to that usually found among MGMCs with work softening [4,5,42]. Actually, for the MGMCs, asynchronized deformation might happen for both phases. Previously, it has been found that a disparity of the elastic limits, Young's moduli, and yield strengths exist for both phases in such kinds of composites [12,28]. Consequently, the dendrites yield preferentially, and plastic deformation starts first within the dendrites, when the matrix is still upon elasticity. Meantime, many DDWs generated in the dendrites begin to develop. Simultaneously, shear bands are poised for the activation and propagation within the matrix. Instead, multiple shear bands with limited length given by the constraints of the crystalline phase form. After both phases enter the plastic deformation stage, the interaction between shear bands and DDWs assists the development of boundaries on the nanoscale at the interface.

Different from the studied by Zhai et al. [27], the moving and pile-up of dislocations in the dendrites induce the formation of DDWs at boundary of the dendrites in the present MGMCs. Furthermore, the interaction between the shear bands and DDWs causes stress concentration at the interface. Since the nanocrystalline structure stems from the interaction between two phases, and is located at the interface. It is clear that the present MGMCs could be divided into three different structures due to the formation of new boundaries after tension. During tension, the work hardening occurred in the dendrites and softening happen in the matrix control the tensile deformation behavior of the dendrites and the matrix, respectively. It results in the intrinsically soft dendrites becoming hard ones, and the relatively hard glass matrix turning into a soft phase. The dendrites show significant work hardening which effectively offsets the work softening of the matrix, and ultimately achieved the excellent work hardening.

4.1. Dislocation pile-ups

Plastic deformation firstly occurs in soft dendrites as soon as multiple dislocations operate during tension. The DDWs in the plastically-deformed dendrites indicate a continuous pile-up of dislocations upon successive straining. Only when dislocation pile-ups develop, i.e., dislocation movement is effectively impeded by grain boundaries [29], twins [14], or interfaces (phase boundaries) [30], successive work-hardening will be available.

To better understand the deformation mechanisms, FEM has been employed to study different parameters corresponding to various dislocation densities in the dendrites. Three defect densities (1×10^7, 5×10^{14}, and $1.5 \times 10^{15}/m^2$) were chosen for the FEM simulations.

Fig. 11 shows the calculated stress-strain curves for different dislocation densities, and the inset shows the corresponding work-hardening rate curve. The results indicate that increasing dislocation densities leads to pronounced work hardening. Fig. 12 displays maps of the dislocation density (left column), the free volume density (center) and strain contours (right) for MGMCs with different dislocation densities in the dendrites at a strain of 5%. The top row corresponds to a dislocation density of $1 \times 10^7/m^2$ in the dendrites, while the middle row displays the results for a dislocation density of $5 \times 10^{14}/m^2$. The bottom images in Fig. 12(g–i) represent the findings for a defect density of $1.5 \times 10^{15}/m^2$. Consistent with our expectations, successive dislocation multiplication and pile-up contribute to the distinct work-hardening in the current composite. Usually, pile-up of dislocations is not achieved and shear banding prevails, accompanied by softening after yielding in the other *in-situ* dendrite-reinforced MGMCs [8,18]. In other words, increasing and pile-up of dislocation are important reasons of the

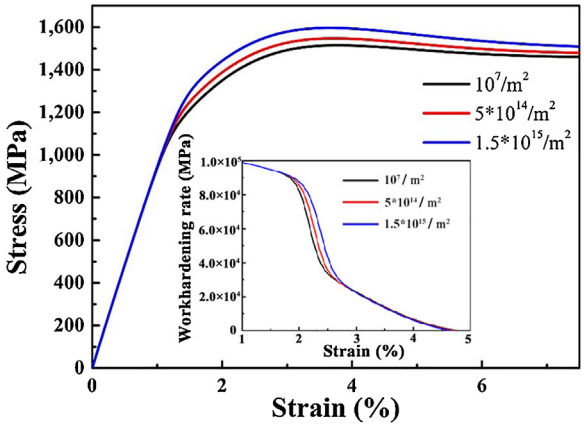

Fig. 11. Calculated true stress-true strain curves of MGMCs with different dislocation densities in the dendrites as obtained by FEM, the inset corresponds to work-hardening curves.

work hardening in such kinds of composites, which is ascribed to the significant work hardening of the dendrites.

4.2. Work-hardening behavior during tension

As reported before, three stages can be found in the deformation stage of MGMCs, i.e., elastic-elastic, elastic-plastic, and plastic-plastic stages [31]. Coincidentally, the tensile strain hardening rate of the present MGMC can be accordingly divided into three stages, as displayed in the inset of Fig. 4(a) and marked as A, B, and C stages. A similar situation can be often found in a variety of crystalline alloys, including Mg-alloys [32], alloys exhibiting transformation-induced plasticity (TRIP) [33], twining-induced plasticity (TWIP) steels [34], and high-entropy alloys (HEAs) [35]. The work-hardening rate first decreases, then remains constant (stage A), and subsequently decreases again (stages B and C) with increasing strain.

At stage A, the dendrites in the present composites have entered the plastic range when the glass matrix still is in the elastic range. The first decrease of the work-hardening rate occurs at the initial state when the dendrites in the composite yield (i.e., the work-hardening rate enters the non-linear deformation stage), which is governed by dislocation glide within the crystalline dendrites. During this stage, the dislocations generated in the dendrites move towards the interface, and pile-up near the interface, as demonstrated in Fig. 5(a) and (b). Meanwhile, dislocations within dendrites can diffuse into the matrix and become absorbed by the matrix. The work-hardening rate in stage A is controlled by the successively increasing dislocation density, effectively restricting dislocation slip. It is noted that the start of stage A at the strain of 0.7%, corresponds to the first inflection point shown in Fig. 6(b), which indicates the yield point of the dendrites. The other point in Fig. 6(b) is regarded as the stage when profuse formation of shear bands in the glass matrix sets in, i.e., the beginning of work softening. At the same time, the multiple dislocations generated within the dendrites move towards the phase boundary, forming DDWs. Loosely bonded free volume regions, which act as flow defects in the glass matrix, can continuously accumulate before the occurrence of plastic deformation. It is noted that softening (i.e., the generation of shear bands) in the glass matrix can be ignored during the elastic-plastic stage. Hence, the plateau of the work-hardening rate in stage A corresponds to stage II in traditional crystalline alloys [22]. It provides an extended work-hardening capacity stretching over about 22% of the whole plastic deformation stage, in a good agreement with crystalline alloys [36]. DDWs and free volume regions appear synchronous near the phase boundary, and cause the formation of the heterogeneous structure at the interface.

After stage A, the propagation of shear bands becomes prevailing at the whole stage B. It has been speculated that the glass matrix generally exhibits softening due to localized structural and ther-

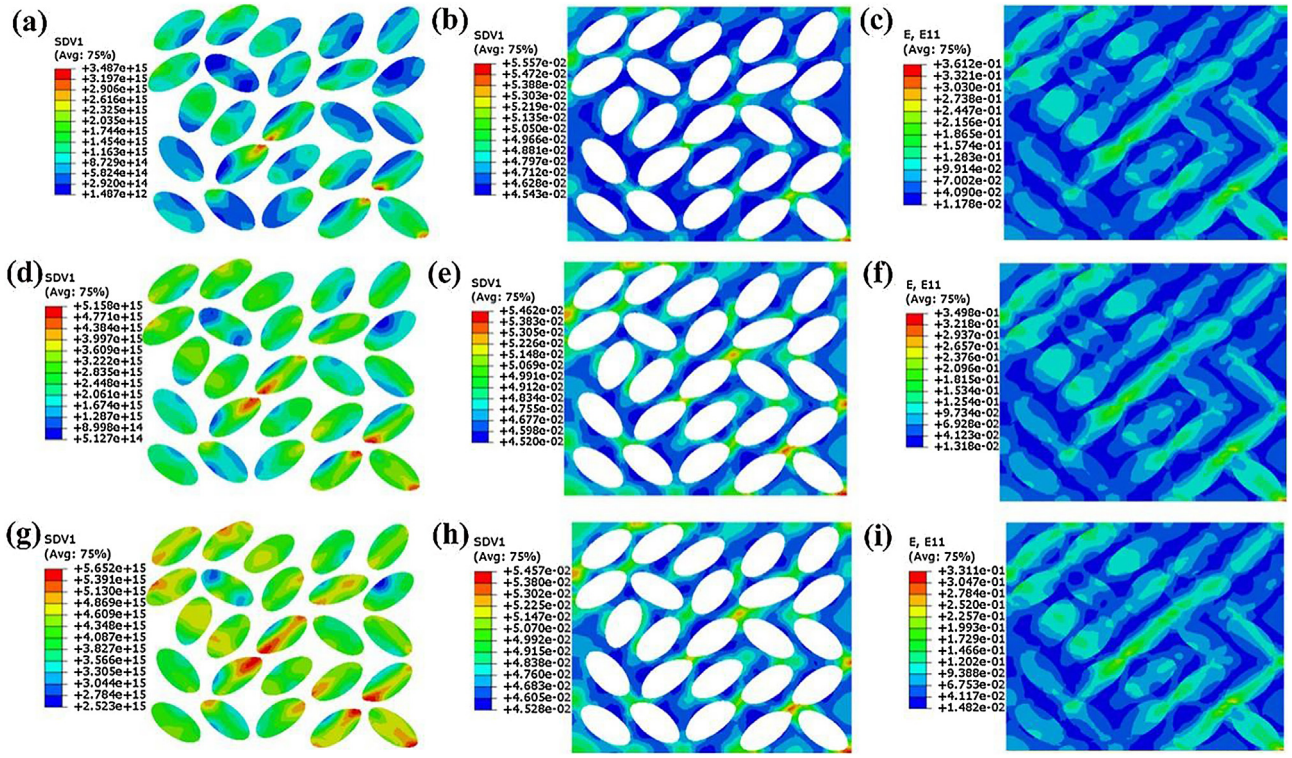

Fig. 12. Free volume density and maps of strain contours of the MGMCs with different defect densities in the dendrites at a true strain of 5%: (a), (b) and (c) $1 \times 10^7/m^2$, (d), (e) and (f) $5 \times 10^{14}/m^2$, (g), (h) and (i) $1.5 \times 10^{15}/m^2$.

Table 3
Hardness of the glass matrix and the dendrites before and after tensile testing measured by nanoindentation.

Type of specimen	Matrix (GPa)	Dendrites (GPa)
As-cast	6.96 ± 0.21	4.58 ± 0.45
Deformed	6.18 ± 0.13	6.22 ± 0.27

mal shearing [1,4]. Accordingly, the work-hardening rate begins to decrease. Nevertheless, the overall deformation behavior remains hardening at this stage. It should be emphasized that the blocking of work-hardened dendrites to the prompt propagation of shear bands is significant, as demonstrated in Fig. 4(b) and 5(d).

With even more plastic straining the dislocation density reaches a dynamic equilibrium state. Dislocation rearrangement becomes active, which is one of the sources for grain boundary migration and the generation of nanocrystals [29,37]. As a result, the interface between the two phases forms a unique boundary structure. The nanoscale boundary in the current work originates from a hierarchical microstructure, not a chemical composition heterogeneous structure, as investigated in Huang's work [38]. The HRTEM and SAED images in Fig. 5(e) show the existence of nanocrystals, which suggests that the interface evolves into boundaries on the nanoscale, and the inner part within dendrites retains the original structure. The heterogeneous structure induced by the formation of special boundaries is particularly beneficial and has an overarching effect on maintaining work hardening in stage B [39]. On one hand, plasticity gradients are built up, which contributes to blocking of the dislocation movement, accompanied by continuous work hardening in dendrites. On the other hand, as reported by Wang et al. [40], the interface between both phases exhibits unique inelastic shear-transfer characteristics, where the glass matrix acts as high-capacity sink enabling the absorption of plasticity. As overall effect, both the successive dislocation pile-up within dendrites and the profuse shear bands in the glass matrix accommodate the plasticity.

Stage C is the final stage, where the work-hardening rate is lower than the true stress [Fig. 4(a)]. Plastic instability occurs at this stage. On the basis of the results in stage B, the glass matrix undergoes pronounced softening upon plastic deformation, which is attributed to shear-induced local dilatation [41]. In contrast, the dendrites are strongly hardened. The boundaries on the nanoscale separate the matrix and the dendrites, and trilaminar heterogeneous structure forms. Meanwhile, the dislocation density generated in the dendrites saturates, which means that defects, such as cracks, have formed in the dendrites at this stage. Hence, multiple mature shear bands appear in the matrix and the dendrites cannot stop them. At this stage, the work-softening mechanisms generated in the glass matrix become more pronounced, while the work-hardening mechanisms generated in the dendrites weaken.

The hardness of the matrix and the dendrites before and after tension have been measured by nanoindentation tests. The Berkovich diamond indenter tip penetrates into the matrix and dendrites, respectively, when conducting nanoindentation tests, and the maximum indentation depth was 1000 μm. At least ten points were selected during the nanoindentation experiments. The results are summarized in Table 3, which verifies the distinctly different deformation behavior of the two phases. The initial hard (glass matrix)/soft (dendrites) model of the MGMC changes into a soft (glass matrix)/hard (dendrites) model after tension, which is caused by the particular deformation mechanisms described above. The excellent work hardening in the dendrites and obvious work softening in the matrix induce the change of hard and soft phases. The nanoscale boundary generates during the process of competition between the dendrites and matrix, which induces the work-hardening behavior occurring in the present MGMC. No macroscopic necking is found, since the composite fails immediately when the plastic instability is reached. On the whole, homogenous plastic elongation is dominant upon tensile loading.

4.3. Constitutive relationship

On the basis of the present and previous findings [14], some implications can be drawn. A transition of different tensile deformation mechanisms corresponding to the various stages upon deformation occurs in the current composites.

At the beginning, both phases of the current composite are in the elastic state, and attempts to derive the Young's moduli for each phase and the composite have been made. Generally, the average Poisson ratio of most BMGs can be assumed as a similar value to crystalline phases [4,42,43]. Hence, for the further considerations the Poisson ratio here is set for 0.33 in both phases [44]. One of the attempts can be established according to Hashin and Shtrikman, as follows [45]:

$$E_c = E_m\left[1+\frac{f_v(E_d-E_m)}{(1-f_v)\beta(E_d-E_m)+E_m}\right], \tag{2}$$

where E_c, E_m, and E_d are the Young's moduli of the composite, the matrix and the dendrites, respectively, the value of f_v is 0.49, which represents the volume fraction of dendrites, β is constant and $\beta=\frac{8-10\nu_m}{15(1-\nu_m)}$, and ν_m (0.33) is the Poisson ratio of the matrix. E_m and E_d are equal to 109 and 83 GPa, respectively. Therefore, E_c can be calculated as 95.5 GPa by inserting these parameters into Eq. (2). Another approach considers simple rule of mixtures (ROM),

$$E_c = E_m(1-f_v)+E_d f_v. \tag{3}$$

The value of E_c is 96.3 GPa, similar to the results obtained by Eq. (2).

With increasing strain, the soft dendrites yield first. On the basis of the ROM, the stress of the composite can be established as:

$$\sigma_c = f_v\sigma_d+(1-f_v)\sigma_m, \tag{4}$$

where σ_c, σ_d, and σ_m are the tensile stresses of the composite, dendrites, and glass matrix, respectively. An overall strain (ε) of 1.5%, a median of this stage, is chosen as an input into Eq. (4), which equates to: $(1-f_v)E_m\varepsilon=(1-0.49)\times109\times0.015=833$ (MPa). Referring to Fig. 4(a), the stress at the strain of 1.5% is about 1200 MPa. As a result, σ_d can be calculated as 749 MPa.

The constitutive equation of the composites at this stage can be expressed according to [46]:

$$\sigma=\frac{1}{\sqrt{3}c_d}\left[\sqrt{3}\sigma_d+3E_m\left(1-\beta\right)\frac{1-f_v}{f_v}\frac{\varepsilon^p}{\sqrt{3}}\right], \tag{5}$$

where c_d and c_m are the average stress-concentration factors of the dendrites and the matrix, respectively ($c_m=\frac{\beta(E_d-E_m)+E_m}{[f_v+(1-f_v)\beta](E_d-E_m)+E_m}$, $c_d=\frac{E_d}{[f_v+(1-f_v)\beta](E_d-E_m)+E_m}$). ε^p is the plastic strain of the composites, which is given as $\varepsilon^p=f_v c_d\varepsilon_d^p$, and ε_d^p is the plastic strain for dendrites. Consequently, Eq. (5) can be written as:$\sigma=\sigma_d+0.28E_m\varepsilon_d^p$. As presented in Fig. 6(b), the yield strain of the dendrites is about 0.7%, and this yield strain of the dendrites in the current MGMC is highly consistent with other Ti-based MGMCs [4,14]. Consequently, the plastic strain of the dendrites, ε_d^p, at the overall strain of 1.5% is about 0.8%. According to Eq. (5), the stress acting on the dendrites at the overall strain of 1.5% is calculated as 950 MPa, very close to the stress in dendrites in other Ti-based MGMCs and Ti-based crystalline alloys [4,22]. The model in Eq. (5) is more suitable for interpreting the stress conditions at this stage. The yield stress for the dendrites is about 580 MPa, according to Hooke's law. The work-hardening exponent,n, is estimated to be 0.66.

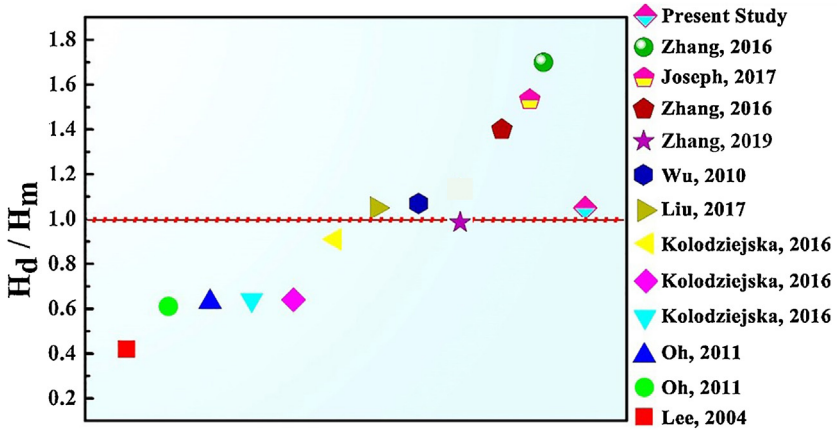

Fig. 13. Ratios of the hardness of the dendrites (H_d) and the matrix (H_m) for different MGMCs.

Both phases undergo plastic deformation at this stage when the glass phase begins to yield. This stage corresponds to the decrease of the work-hardening rate, as shown in Fig. (4 b). For a dislocation-free crystal, it has been postulated by Frenkel that the theoretical shear strength can be assumed to be $\tau_y \cong G/5$. Therefore, the yield strength of the glass matrix can be calculated as 1640 MPa ($\sigma_{ym} = 2\tau_y$) [47]. The tensile stress of the current composite in this stage is given by [46]:

$$\sigma = \frac{1}{\sqrt{3}c_m}\left[\sqrt{3}\sigma_{ym} - 3E_m(1-\beta)\frac{\varepsilon^p}{\sqrt{3}}\right], \quad (6)$$

and Eq. (6) can be simplified as:$\sigma = \sigma_{ym} - 0.524E_m\varepsilon^p$. In another way, the tensile stress-strain relation of the matrix in the stage C can be represented as [46]:

$$\sigma = \sigma_{ref}(\sigma_{ym}/E_m + \epsilon^p)^{n'}, \quad (7)$$

where σ_{ref} is the reference stress of the matrix during uniaxial tension, and $\sigma_{ref} = \frac{E_m^{n'}}{\sigma_{ym}^{n'-1}}$, n' is the work-hardening coefficient of the matrix. The work-softening strain of the stage C can be inferred at a strain of 3.0% [Fig. 4(a)], which is close to the second inflection point displayed in Fig. 6(b). Combining Eqs. (6) and (7), the work-hardening coefficient of the matrix at this stage can be calculated as - 0.069. This trend indicates that the work-hardening in the dendrites is more pronounced than the softening induced in the glass matrix, which results in the excellent work hardening in the current composite. Such a situation is in line with the experimental data (cf. Table 3). The introduction of ductile dendrites with significant work hardening is an effective route to achieve work hardening upon tension of the MGMCs, the hardening of the dendrites can surpass work softening of the matrix. During tension, the hardness of the dendrites and the matrix show opposite trends, the hardness of the dendrites increase while the hardness of the matrix decrease. In the present MGMCs, Table 3 reveals that the hardness of the matrix decreases while that of the dendrites increases upon tensile deformation. The dendrite hardness becomes higher than that of the glass matrix, suggesting that the work-hardening effect overcomes the softening effect. In the present MGMCs, the hardness of the dendrites is higher than that of the matrix after tension. Hence, the ratio of the hardness values of the dendrites to the matrix for a variety of MGMCs with work-hardening ability ($H_d/H_m \geq 1$), is exhibited in Fig. 13 (the literature data were taken from Refs. [48–51]). It means that dendrites with a higher hardness than the matrix are beneficial for work hardening in composites. However, the excellent work-hardening ability of the MGMCs depend on the work hardening of the dendrites. It is note that work hardening can be also achieved among the MGMCs even when the hardness of the dendrites lower than that of the matrix after tension [27].

Furthermore, the FEM results obtained above also confirm the conclusions. The deformation behavior of dendrite 1–3 can be regarded as different deformation stages of MGMC 2 during tension. Dendrite 1 presents the initial state, and dendrite 3 correspond to the final state induced by work hardening (dendrite 2). The MGMC 1 with soft dendrite 1 displays work softening and a shear-localization distribution occurred during deformation [Fig. 10 (c)]. On the other hand, the MGMC 3 with the hard dendrite 3 shows similar local stress distributions [Fig. 10 (f) and (i)], which indicates that the hard dendrite phase within the matrix makes MGMCs hardening. The MGMC 2 in FEM is based on the present composite, showing dendrites change from soft to hard phase during tension. And the corresponding work hardening will be achieved at the same time. Hence, it is reasonable to rationalize that the work-hardening capacity in the present composite is a result of the pronounced hardening of the dendrites.

5. Conclusion

In the previous work, the deformation mechanisms of the $Ti_{41}Zr_{32}Ni_6Ta_7Be_{14}$ MGMC have been revealed and characterized by experiments and theoretical calculations. The work-hardening behavior in the dendrites is ascribed to the formation of boundaries on the nanoscale, which are induced by generating DDWs during tensile deformation. On the other hand, softening in the matrix is induced by the formation of shear bands. Combining these factors, the stress condition of the current composites has been studied step by step according to the three deformation stages, thus revealing an overall homogeneous plastic deformation mechanism. Obviously, the work-hardening ability of the dendrites overcomes the softening of the glass matrix and leads to a significantly homogeneous tensile elongation.

Acknowledgements

J.W.Q. acknowledges the financial supports of the National Natural Science Foundation of China (No. 51371122), the Natural Science Foundation of Shanxi Province, China (No. 201901D111105), and the Transformation of Scientific and Technological Achievements Programs of Higher Education Institutions in Shanxi (2019). P.K.L. is very grateful for the support from the National Science Foundation (DMR-1611180 and 1809640) with the program directors, Drs. G. Shiflet and D. Farkas. D.Ş. acknowledges the financial support by the German Science Foundation (DFG) through the grant SO 1518/1-1. J.E. and D.Ş. would like to acknowledge the support through the ERC

Advanced Grant INTELHYB (grant ERC-2013-ADG-340025). D.K. would like to acknowledge the support by the European Research Council under the ERC Grant Agreement (No. 771146 TOUGHIT).

References

[1] W.L. Johnson, MRS Bull. 24 (1999) 42–56.
[2] W.H. Wang, C. Dong, C.H. Shek, Mater. Sci. Eng. R 44 (2004) 45–89.
[3] C. Schuh, T. Hufnagel, U. Ramamurty, Acta Mater. 55 (2007) 4067–4109.
[4] J.W. Qiao, H. Jia, P.K. Liaw, Mater. Sci. Eng. R 100 (2016) 1–69.
[5] Y.Y. Liu, P.Z. Liu, J.J. Li, P.K. Liaw, F. Spieckermann, D. Kiener, J.W. Qiao, Int. J. Plast. 105 (2018) 225–238.
[6] Z. Liu, R. Li, G. Liu, W. Su, H. Wang, Y. Li, M. Shi, X. Luo, G. Wu, T. Zhang, Acta Mater. 60 (2012) 3128–3139.
[7] Y. Wu, Y. Xiao, G. Chen, C.T. Liu, Z. Lu, Adv. Mater. 22 (2010) 2770–2773.
[8] Y.Y. Liu, J.J. Li, Z. Wang, X.H. Shi, J.W. Qiao, Y.C. Wu, Intermetallics 108 (2019) 72–76.
[9] K.K. Song, S. Pauly, Y. Zhang, R. Li, S. Gorantla, N. Narayanan, U. Kühn, T. Gemming, J. Eckert, Acta Mater. 60 (2012) 6000–6012.
[10] Y.S. Oh, C.P. Kim, S. Lee, N.J. Kim, Acta Mater. 59 (2011) 7277–7286.
[11] L. Zhang, W.Q. Li, Z.W. Zhu, H.M. Fu, H. Li, Z.K. Li, H.W. Zhang, A.M. Wang, H.F. Zhang, J. Mater. Sci. Technol. 33 (2017) 708–711.
[12] L. Zhang, R.L. Narayan, H.M. Fu, U. Ramamurty, W.R. Li, Y.D. Li, H.F. Zhang, Acta Mater. 168 (2019) 24–36.
[13] F. Szuess, C.P. Kim, W.L. Johnson, Acta Mater. 49 (2001) 1507–1513.
[14] J. Fan, J.W. Qiao, Z.H. Wang, W. Rao, G.Z. Kang, Sci. Rep. 7 (2017) 1877.
[15] W. Rao, J. Zhang, G.Z. Kang, C. Yu, H. Jiang, Int. J. Plast. 115 (2019) 238–267.
[16] Y. Jiang, X. Shi, K. Qiu, Mater. Des. 77 (2015) 32–40.
[17] W. Rao, J. Zhang, H. Jiang, G.Z. Kang, Mech. Mater. 103 (2016) 68–77.
[18] C.C. Hays, C.P. Kim, W.L. Johnson, Phys. Rev. Lett. 84 (1999), 2901-1904.
[19] L. Zhang, Z. Zhu, H. Fu, H. Li, H. Zhang, Mater. Sci. Eng. A 689 (2017) 404–410.
[20] D. Banerjee, J.C. Williams, Acta Mater. 61 (2013) 844–879.
[21] M. Marteleur, F. Sun, T. Gloriant, P. Vermaut, P.J. Jacques, F. Prima, Scripta Mater. 66 (2012) 749–752.
[22] G.E. Dieter, in: F.M. Robert (Ed.), Mechanical Metallurgy, McGraw-Hill, London, 1961, p. 290.
[23] X. Li, R. Song, N. Zhou, J. Li, Scripta Mater. 154 (2018) 30–33.
[24] C.L. Yang, Z.J. Zhang, P. Zhang, Z.F. Zhang, Acta Mater. 136 (2017) 1–10.
[25] Z.F. Zhang, J. Eckert, L. Schultz, Acta Mater. 51 (2003) 1167–1179.
[26] Y. Shao, K. Yao, M. Li, X. Liu,Appl. Phys. Lett. 103 (2013), 171901.
[27] H.M. Zhai, H.F. Wang, F. Liu, J. Alloys. Compd. 685 (2016) 322–330.
[28] H. Zhai, Y. Xu, F. Zhang, Y. Ren, H. Wang, F. Liu, J. Alloys. Compd. 694 (2017) 1–9.
[29] L.S. Tóth, Y. Estrin, R. Lapovok, C. Gu, Acta Mater. 58 (2010) 1782–1794.
[30] W. Guo, E. Jägle, J. Yao, V. Maier, S. Korte-Kerzel, J.M. Schneider, D. Raabe, Acta Mater. 80 (2014) 94–106.
[31] J.W. Qiao, J. Mater. Sci. Technol. 29 (2013) 685–701.
[32] S.B. Yi, C.H.J. Davies, H.G. Brokmeier, R.E. Bolmaro, K.U. Kainer, J. Homeyer, Acta Mater. 54 (2006) 549–562.
[33] O. Grässel, L. Krüger, G. Frommeyer, L.W. Meyer, Int. J. Plast. 16 (2000) 1391–1409.
[34] B.C. De Cooman, Y. Estrin, S.K. Kim, Acta Mater. 142 (2018) 283–362.
[35] L. Ma, L. Wang, Z. Nie, F. Wang, Y. Xue, J. Zhou, T. Cao, Y. Wang, Y. Ren, Acta Mater. 128 (2017) 12–21.
[36] V.S.A. Challa, X.L. Wan, M.C. Somani, L.P. Karjalainen, R.D.K. Misra, Scripta Mater. 86 (2014) 60–63.
[37] K.Y. Zhu, A. Vassel, F. Brisset, K. Lu, J. Lu, Acta Mater. 52 (2004) 4101–4110.
[38] E.W. Huang, J. Qiao, B. Winiarski, W.J. Lee, M. Scheel, C.P. Chuang, P.K. Liaw, Y.C. Lo, Y. Zhang, M.D. Michiel, Sci. Rep. 4 (2014) 4394.
[39] F. Roters, D. Raabe, G. Gottstein, Acta Mater. 48 (2000) 4181–4189.
[40] Y. Wang, J. Li, A.V. Hamza, T.W. Barbee, Proc. Natl. Acad. Sci. U. S. A. 104 (2007) 11155–11160.
[41] H. Bei, S. Xie, E.P. George,Phys. Rev. Lett. 96 (2006), 105503.
[42] X.H. Sun, J.W. Qiao, Z.M. Jiao, Z.H. Wang, H.J. Yang, B.S. Xu, Sci. Rep. 5 (2015) 13964.
[43] D.P. Wang, S.L. Wang, J.Q. Wang, Corros. Sci. 59 (2012) 88–95.
[44] W.H. Wang, Prog. Mater. Sci. 57 (2012) 487–656.
[45] Z. Hashin, J. Mech. Phys. Solids. 11 (1963) 127–140.
[46] S.H. Xia, J.T. Wang, Int. J. Plast. 26 (2010) 1442–1460.
[47] W.L. Johnson, K. Samwer,Phys. Rev. Lett. 95 (2005), 195501.
[48] J. Joseph, N. Stanford, P. Hodgson, D.M. Fabijanic, J. Alloys. Compd. 726 (2017) 885–895.
[49] J.A. Kolodziejska, H. Kozachkov, K. Kranjc, A. Hunter, E. Marquis, W.L. Johnson, K.M. Flores, D.C. Hofmann, Sci. Rep. 6 (2016) 22563.
[50] J.C. Lee, Y.C. Kim, J.P. Ahn, H.S. Kim, S.H. Lee, B.J. Lee, Acta Mater. 52 (2004) 1525–1533.
[51] L. Zhang, H.F. Zhang, W.Q. Li, T. Gemming, Z.W. Zhu, H.M. Fu, J. Eckert, S. Pauly, Scripta Mater. 125 (2016) 19–23.